

This is a self-archived version of an original article. This version may differ from the original in pagination and typographic details.

Author(s): Ghiyasi, Ramin; Philip, Anish; Liu, Ji; Julin, Jaakko; Sajavaara, Timo; Nolan, Michael; Karppinen, Maarit

Title: Atomic Layer Deposition of Intermetallic Fe₄Zn₉ Thin Films from Diethyl Zinc

Year: 2022

Version: Published version

Copyright: © The Authors. Published by American Chemical Society

Rights: CC BY 4.0

Rights url: <https://creativecommons.org/licenses/by/4.0/>

Please cite the original version:

Ghiyasi, R., Philip, A., Liu, J., Julin, J., Sajavaara, T., Nolan, M., & Karppinen, M. (2022). Atomic Layer Deposition of Intermetallic Fe₄Zn₉ Thin Films from Diethyl Zinc. *Chemistry of Materials*, 34(11), 5241-5248. <https://doi.org/10.1021/acs.chemmater.2c00907>

Atomic Layer Deposition of Intermetallic Fe₄Zn₉ Thin Films from Diethyl Zinc

Ramin Ghiyasi, Anish Philip, Ji Liu, Jaakko Julin, Timo Sajavaara, Michael Nolan, and Maarit Karppinen*

Cite This: <https://doi.org/10.1021/acs.chemmater.2c00907>

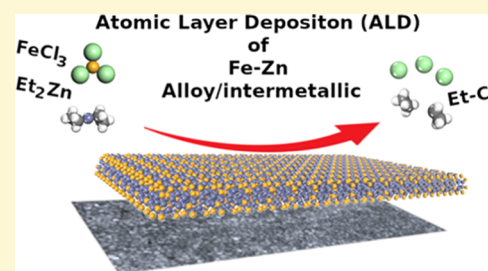
Read Online

ACCESS |

Metrics & More

Article Recommendations

ABSTRACT: We present a new type of atomic layer deposition (ALD) process for intermetallic thin films, where diethyl zinc (DEZ) serves as a coreactant. In our proof-of-concept study, FeCl₃ is used as the second precursor. The FeCl₃ + DEZ process yields in situ crystalline Fe₄Zn₉ thin films, where the elemental purity and Fe/Zn ratio are confirmed by time-of-flight elastic recoil detection analysis (TOF-ERDA), Rutherford backscattering spectrometry (RBS), atomic absorption spectroscopy (AAS), and energy-dispersive X-ray spectroscopy (EDX) analyses. The film thickness is precisely controlled by the number of precursor supply cycles, as expected for an ALD process. The reaction mechanism is addressed by computational density functional theory (DFT) modeling. We moreover carry out preliminary tests with CuCl₂ and Ni(thd)₂ in combination with DEZ to confirm that these processes yield Cu–Zn and Ni–Zn thin films with DEZ as well. Thus, we envision an opening of a new ALD approach based on DEZ for intermetallic/metal alloy thin films.



1. INTRODUCTION

Atomic layer deposition (ALD) is the fastest growing thin-film technology in microelectronics and beyond, owing to the superior film characteristics it provides.^{1–6} In a prototype ALD process, two different gaseous/vaporized precursors are sequentially pulsed and purged out of the reaction chamber with prespecified time intervals.^{7,8} The precursor pulse and purge times are selected so that the precursors have enough time to chemisorb on the surface and react with the available surface groups for full surface coverage. Another important feature is the self-limitation of the surface reactions such that the chemisorption of one precursor is limited to a monolayer; the reaction only continues after the excess precursor molecules from the gas phase are purged out and the second precursor is delivered to the reaction chamber. As the two precursors are not present at the same time in the chamber, no unwanted gas-phase reactions occur. This unique growth process leads to highly uniform and conformal thin films with atomic-level control of both thickness and composition.

Most commonly the ALD technique is applied to the fabrication of binary metal oxide (e.g., Al₂O₃, HfO₂, TiO₂, ZnO),^{9,10} sulfide (e.g., ZnS),^{1,11} or nitride (e.g., Si₃N₄)¹² thin films; in these depositions, the second precursor is the source of oxygen (e.g., H₂O, O₃), sulfur (e.g., H₂S, S), or nitrogen (e.g., NH₃). Ternary and even quaternary processes are possible as well, but these are more challenging to optimize.^{13–15} More recently, the interest in ALD of pure metals has been rapidly increasing.^{16,17} Here, the major challenges are related to finding the optimal conditions for the reduction of the metal cations and tackling the agglomeration/island growth issues, leading to rough and

even discontinuous films. In the case of noble metals, specific reductants are not always needed; a renowned example in combustion reactions of platinum-group metal precursors is oxygen.¹⁸ For the non-noble metals, molecular H₂ is the most common reducing agent.¹⁹ However, its limited reactivity is a major challenge. Hydrogen plasma is another possibility,²⁰ but a common difficulty is the film conformality. More recently, different organic reactants have been investigated as well for the growth of metal films.^{21,22}

Considering the challenges with the ALD fabrication of single-metal thin films, it is not surprising that the application of ALD in depositing multimetal (metal alloys or intermetallic compounds) is limited to a few successful examples only.^{23–26} The highlights in this area include the pioneering work of Christensen and Elam²³ in depositing Ir–Pt alloys from Ir(III) acetylacetonate/O₂ and (trimethyl)methylcyclopentadienyl Pt(IV)/O₂ cycles, and the more recent successes by Väyrynen et al.^{24–26} in depositing Co₃Sn₂, Ni₃Sn₂, and Ni₂Ge films using carbene metal hydrides with a metal–hydrogen bond as a reductant. Hydrides have also been used to deposit single-metal Al films.²⁷

Herein, we introduce a novel ALD approach not relying on hydrogen or hydride species for multimetal thin films. The

Received: March 25, 2022

Revised: May 5, 2022

process is based on one of the most common ALD precursors, that is, diethyl zinc (DEZ) extensively used for the growth of ZnO films.¹⁰ It should be noted that there are a couple of reports on the use of DEZ as a reductant for pure metallic films;^{28–31} interestingly, depending on the deposition temperature, some unintended inclusions of Zn deposits in the Cu films were observed in these films occasionally. Now, we demonstrate that when combining DEZ with FeCl₃—another well-behaving ALD precursor—^{32,33,33,33} we can deposit in situ crystalline iron–zinc intermetallic films in a controlled manner. Here, we may see some similarities to the works by Xiang et al.^{34–36} who deposited Ti–Al films from trimethylaluminum (TMA) and TiCl₄. However, in these films, the carbon contamination was so high that the films were closer to the Ti–Al–C carbide composition. We also like to mention that in another somewhat similar process, Pore et al.³⁷ deposited Sb and Ge telluride films from chloride and trialkylsilyl precursors.

There are five intermetallic compounds reported in the Zn–Fe system, in the order of increasing Fe content: ζ (FeZn₁₃), $\delta 1p$ (Fe₁₃Zn₁₂₆), $\delta 1k$ (FeZn₇), $\Gamma 1$ (Fe₁₁Zn₄₃), and Γ (Fe₄Zn₉).^{38,39} Among these, the γ -Fe₄Zn₉ phase with the highest Fe content and a bcc-type crystal structure is probably the best established one and also the product of our ALD process. In the literature, the γ -Fe₄Zn₉ phase has been reported to form with the lower Fe/Zn ratios of FeZn₃ and Fe₃Zn₁₀ as well.^{38,39} This seems to be the case with the present study too. In automotive and other industries, Fe–Zn layers are conventionally produced through electroplating on galvanized steel or other metal surfaces, e.g., for anticorrosive or mechanical coatings.^{40–42} More recently, Zn–Fe coatings have been investigated, for example, as biodegradable medical coatings on implants,^{43,44} where the ALD technique could offer unique advantages.

2. EXPERIMENTAL SECTION

Fe–Zn thin films were deposited in a flow-type thermal ALD reactor (ASM Microchemistry F120) on 2 × 2 cm² glass and silicon substrates. For the depositions, the FeCl₃ precursor powder (Merck, 95%) was placed inside the reactor and heated at 158 °C for sublimation, while the DEZ precursor (Zn(CH₂CH₃)₂; Sigma-Aldrich, ≥52 wt % Zn basis) bottle was kept outside the reactor at room temperature. Nitrogen (99.999%; N₂ 5.0) was used as the carrier and purge gas. It should be emphasized that no other reactants were employed, and the reactor was kept under a constant vacuum (2.6 mbar). The depositions totaled a fixed number of cycles (100, unless otherwise stated), and each cycle consisted of the following four gas pulses: DEZ precursor, N₂ purge, FeCl₃ precursor, and N₂ purge. The purge time was always twice the precursor pulse time to make sure that all of the possible leftover materials from the previous pulse were eliminated from the gas phase; to be sure that this purge length was long enough, we investigated also shorter (1.5 times) and longer (4 times) purges to confirm that the film growth rates remained the same.

Profilometry (Veeco Dektak 6M stylus profilometer) and X-ray reflectivity (XRR; Panalytical XPert diffractometer, Cu K α source) methods were utilized to determine the film thicknesses. The surface morphology was studied by scanning electron microscopy (SEM; Hitachi S-4700). The crystallinity and phase composition of the films were investigated by grazing incidence X-ray diffraction (GIXRD; incidence angle of 0.5°; the same diffractometer as for XRR).

The chemical composition of the films was addressed through several different approaches—using both easily accessed in-house techniques and more advanced characterization tools—to get a comprehensive view, as the different techniques were assumed to complement each other regarding the information they provide. Atomic absorption spectroscopy (AAS; Varian AA240) was used as

the first tool to routinely check the samples for the Fe/Zn ratio. For the AAS analysis, the films were deposited on a glass substrate from which the film material could be quantitatively dissolved in nitric acid, followed by dilution with water; each analysis was repeated three times to obtain the Fe/Zn ratio with an appreciable certainty. Some of the samples were also investigated during the initial process development to rule out the Cl contamination (and also for the semiquantitative Fe/Zn ratio) by energy-dispersive X-ray spectroscopy (EDX; Tescan Mira 3). In the EDX measurements, the elemental mapping was carried out on the entire substrate to also address the homogeneity of the films. Later, the Fe/Zn ratios were measured using Rutherford backscattering spectrometry (RBS) and time-of-flight elastic recoil detection analysis (TOF-ERDA) for a selection of films grown on silicon substrates. Most importantly, from the ERDA measurements, the light-element (C, O, Cl) contamination level could be accurately addressed. The RBS measurements were carried out by the application of a ⁴He^{1+/2+} beam with 2 and 3 MeV energies and TOF-ERDA measurements using an 11.9 MeV ⁶³Cu⁷⁺ ion beam from a 3 × 3 mm² surface area.

To address the surface reactions, computational calculations were performed on the basis of periodic spin-polarized density functional theory (DFT) within a plane-wave basis set and projector augmented wave (PAW) formalism, as implemented in the Vienna Ab initio Simulation Package (VASP 5.3) code.⁴⁵ The generalized gradient approximation (GGA) with the parameterization of Perdew–Burke–Ernzerhof (PBE) was used for the exchange–correlation functional.^{46,47} The plane-wave energy cutoff was set to be 400 eV. The valence electrons were 12 for Zn, 8 for Fe, 7 for Cl, 4 for C, and 1 for H. The convergence of energy and forces were set to be 1 × 10^{−4} eV and 0.02 eV/Å, respectively. A *k*-point mesh⁴⁵ of 3 × 3 × 1 was used throughout the calculations. The unit cell of Fe₄Zn₉, shown in Figure 1, was obtained from Material Project.⁴⁸ The lattice constant was *a* =

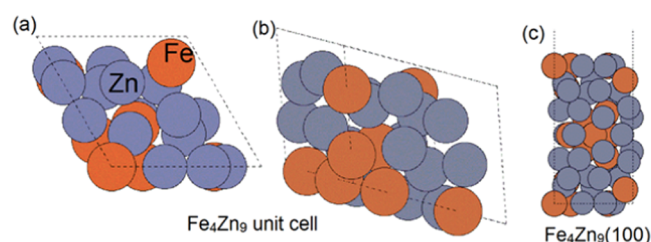


Figure 1. Configurations of (a) top view and (b) side view of the Fe₄Zn₉ unit cell and (c) Fe₄Zn₉(100); zinc and iron atoms are represented by dark gray and orange colors.

b = *c* = 7.77 Å. The slab model of Fe₄Zn₉(100) had 20 Fe atoms and 40 Zn atoms, where all of the atoms were allowed to relax. A 15 Å vacuum region was applied. The molecular geometries of precursor FeCl₃ and DEZ (Zn(Et)₂) and byproducts were relaxed in the same supercell as the slab model of Fe₄Zn₉, with an energy cutoff of 400 eV and γ point sampling. The van der Waals correction was applied with the PBE-D3 method to ensure an accurate description of the metal precursor adsorption energy. The adsorption energy was calculated from

$$E_{\text{ad}} = E_{\text{tot}} - E_{\text{subs}} - E_{\text{A}}$$

where E_{tot} , E_{subs} , and E_{A} are the energy of the slab with precursors, the slab model for Fe₄Zn₉, and isolated precursors or the byproduct, respectively.

3. RESULTS

All our depositions from DEZ and FeCl₃ yielded visually homogeneous crystalline thin films for which no other elements than zinc and iron were detected from the EDX analysis. The homogeneity was additionally confirmed by the EDX mapping over the entire surface area. For representative samples, the light-element (C, O, Cl) impurity levels were

analyzed in detail using TOF-ERDA, see Figure 2 for a depth profile. On the very surface of the films, TOF-ERDA detects of

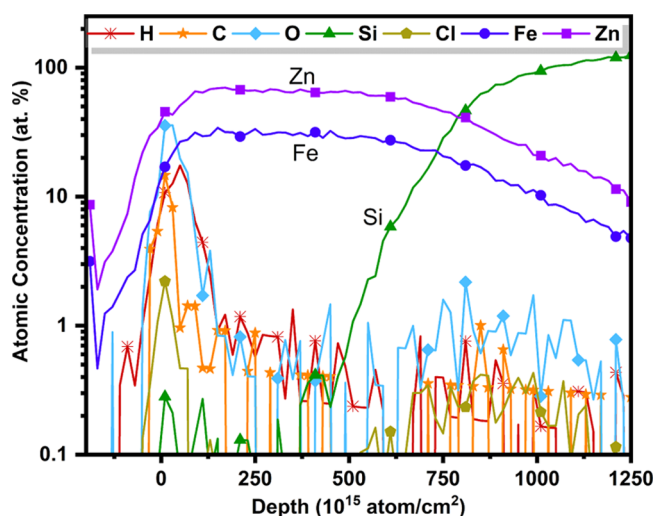


Figure 2. Elemental depth profile obtained with TOF-ERDA, for example, the thin-film sample deposited at 260 °C.

C, O, and Cl (presumably due to the incomplete loss of precursor ligands) were observed, but deeper in the bulk, the films have impurity concentrations well below 1 atom % for H, C, and O. From both AAS and RBS analysis, all of the films contained iron and zinc, the Fe/Zn ratio slightly varying depending on the deposition conditions. The GIXRD patterns indicated that γ -Fe₄Zn₉ was the main phase in all samples, with a minority Fe metal phase in the Fe-rich region. No indication of Zn metal was seen for any of the samples; this is an important note, as DEZ has been seen to decompose into metallic Zn in some ALD processes at high temperatures and with long DEZ pulses.⁴⁹ Also, we confirmed that no film growth occurred when DEZ was pulsed alone into the reactor.

We investigated our DEZ + FeCl₃ process systematically against various deposition parameters; the results are summarized in Figure 3. The influence of the deposition temperature on the growth-per-cycle (GPC) value is shown in Figure 3A for the range of 240–300 °C; outside of this temperature range, the films were found to be nonuniform. In these experiments, the precursor pulse lengths were kept unchanged at 2 s DEZ and 2 s FeCl₃. The tiny increase in GPC

with temperature seen in Figure 3A could be explained by the fact that we also observed minor changes in the Fe/Zn ratio in AAS measurements, the Zn content slightly increasing with increasing deposition temperature.

One of the cornerstones of an ALD process is the saturation of the surface reactions within each precursor pulse. This is typically demonstrated by showing that the GPC value first increases and then saturates upon increasing the precursor pulse lengths. In Figure 3B, we demonstrate this for our DEZ + FeCl₃ process by plotting the GPC value against the pulse lengths of the two precursors, one varied at the time, while keeping the other fixed (at 4 s for FeCl₃ and at 2 s for DEZ). These experiments were carried out while keeping other process parameters fixed, i.e., the deposition temperature at 260 °C and the number of cycles at 100. It should be noted that we carried out additional experiments where we tested other pulse length combinations as well to verify that the saturation behavior for one of the precursor pulse lengths was not sensitively depending on the choice of the pulse length for the other. From Figure 3B, we can see that the initially chosen pulse lengths of 4 s for FeCl₃ and 2 s for DEZ are long enough to reach saturation. The growth rate saturates to the relatively high GPC value of ca. 9.0 Å/cycle, which is—interestingly—close to the lattice parameter (8.982 Å)⁴² of the γ -Fe₄Zn₉ phase. This is likely to result from the highly exothermic reactions involved in the deposition of FeZn from FeCl₃ and DEZ, as described in Section 4.

Another important criterion for an ALD process is the growth linearity in terms of the number of precursor pulsing cycles applied. Figure 3C illustrates this for the present FeCl₃ + DEZ process. For these experiments, the precursor pulse lengths were fixed to 4 s for FeCl₃ and 2 s for DEZ, and the deposition temperature was 260 °C.

We then characterized the resultant Zn–Fe films for their elemental and crystalline phase compositions. In Figure 4, GIXRD patterns are displayed for three representative 78–93 nm thick samples, all deposited at 260 °C but with somewhat different precursor pulse lengths, together with simulated reference patterns for γ -Fe₄Zn₉ and α -Fe.^{50,51} Table 1 lists the atomic Fe/Zn ratios for the same samples as obtained from the RBS, AAS, and EDX analyses. Among the three techniques, RBS is the most accurate, while EDX is considered only semiquantitative, and moreover surface sensitive. The absolute values from the different techniques do not match perfectly but the trends are quite similar though, i.e., the Fe content

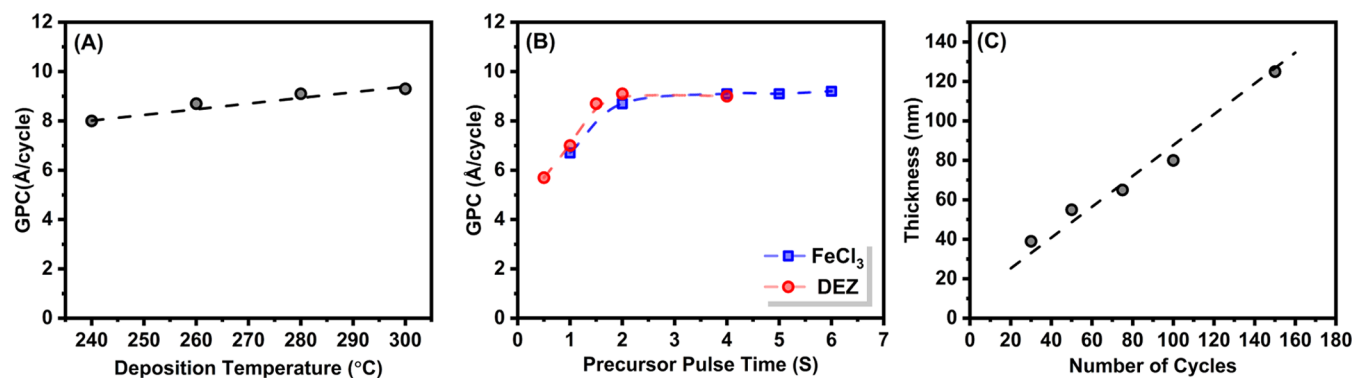


Figure 3. Characteristics of the DEZ + FeCl₃ process: (A) GPC value versus deposition temperature, (B) GPC value versus precursor pulse lengths for both precursors, and (C) film thickness versus the number of deposition cycles. In (A) and (B), the number of cycles was 100. In (B) and (C), the deposition temperature was 260 °C; the GPC values are from profilometry data.

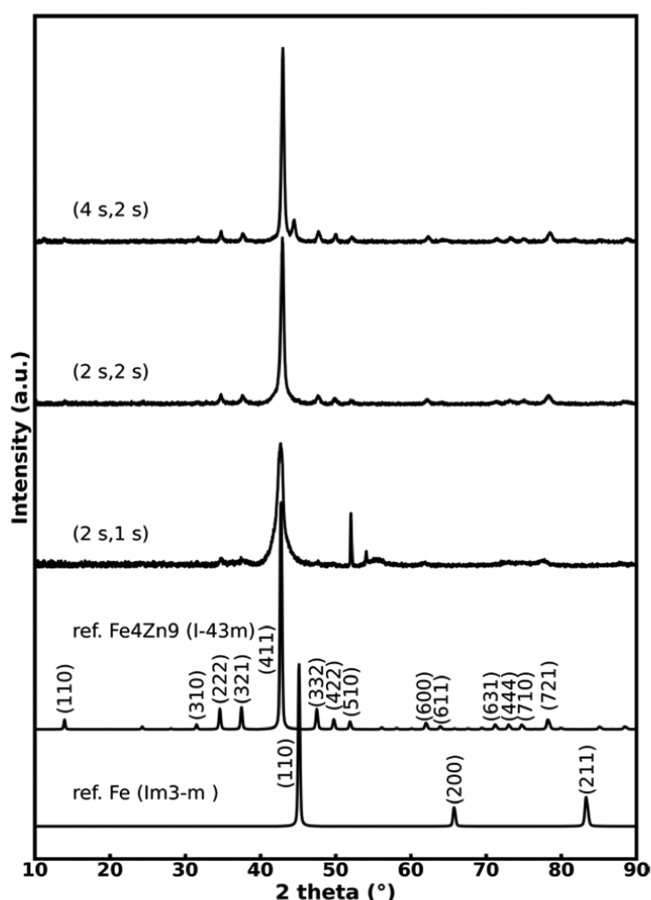


Figure 4. GIXRD patterns for the Fe–Zn films grown at 260 °C with different precursor pulse lengths, together with indexed reference XRD patterns for γ - Fe_4Zn_9 and α -Fe; peaks in the range seen for the (2 s, 1 s) sample in the 50–60° area are due to the Si substrate.

Table 1. Atomic Fe/Zn Ratio Estimated from RBS, AAS, and EDX Analyses for the Fe–Zn Films Grown at 260 °C with Different Precursor Pulse Lengths

sample (FeCl ₃ , DEZ)	RBS	AAS	EDX
(4 s, 2 s)	0.51	0.39	0.6
(2 s, 2 s)	0.19	0.32	0.5
(2 s, 1 s)	0.12	0.15	0.2

increases with increasing precursor pulse lengths. Here, we should recall that among the three samples, only the one with the longest precursor pulses (4 s FeCl₃, 2 s DEZ) was grown in an area clearly fulfilling the surface saturation conditions (Figure 3).

From Figure 4, while the Fe₄Zn₉ phase dominates all of the three GIXRD patterns, the film deposited with the shortest precursor pulse lengths (2 s FeCl₃, 1 s DEZ) shows the broadest diffraction peaks, i.e., the lowest degree of crystallinity. Also, the elemental Fe/Zn ratio for this sample is clearly below the “stoichiometric” value of 0.44 assumed for Fe₄Zn₉ (although based on the previous literature, the Fe₄Zn₉ phase may be stabilized over a relatively wide compositional range, even down to the Fe/Zn ratio of 0.30).^{38,39} On the other hand, for the sample deposited with the longest precursor pulse lengths (4 s FeCl₃, 2 s DEZ), the values obtained for the Fe/Zn ratio with the different analysis techniques are quite close to the ideal 0.44 value (Table 1).

However, for this sample, a trace of the α -Fe phase is distinguished from the GIXRD pattern. The highest Fe₄Zn₉ phase purity is seen for the sample deposited with the pulse lengths 2 s for FeCl₃ and 2 s for DEZ. The density value determined for this highly crystalline and essentially single-phase Fe₄Zn₉ sample from the XRR fitting (7 g/cm³) is quite close to the ideal value of 7.44 g/cm³ calculated from the crystal structure data for γ -Fe₄Zn₉. The Fe/Zn value (from the most accurate RBS/TOF-ERDA analysis) for this sample appears a little low against the nominal Fe₄Zn₉ stoichiometry; unfortunately, the reason for this could not be clarified within this study.

We also addressed the surface morphology of the most phase-pure and highly crystalline sample by measuring its surface profile using profilometry (Figure 5). The film

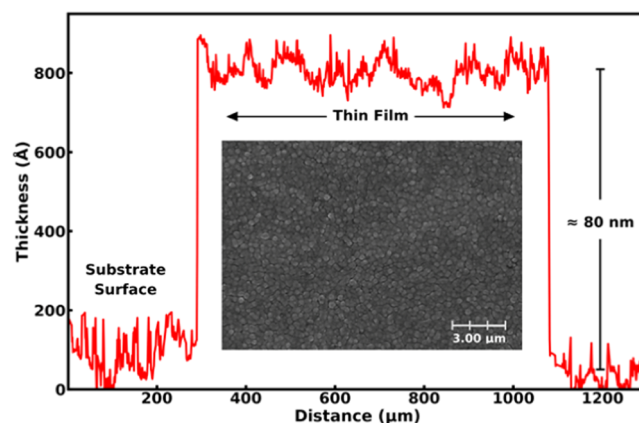


Figure 5. Surface profile and the SEM image for the Fe–Zn film deposited at 260 °C (2 s, 2 s).

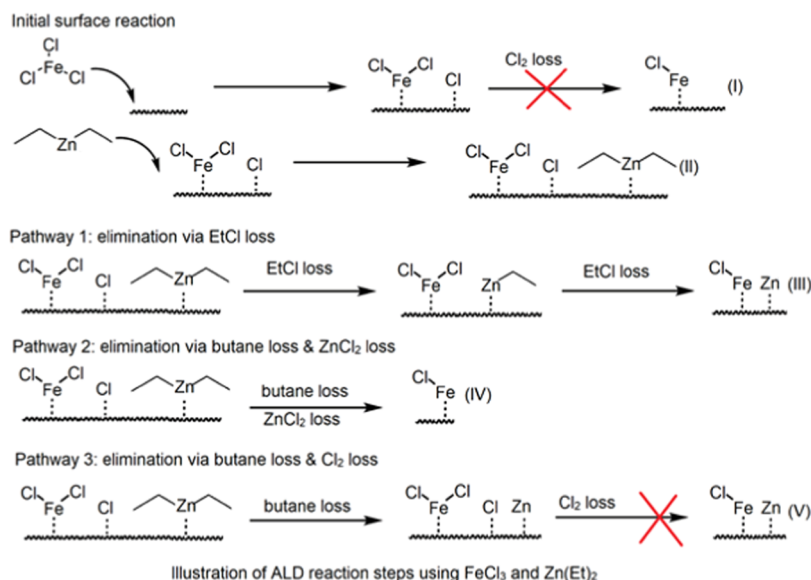
thickness is obtained at ca. 80 nm in good agreement with the XRR-based estimation, and the small fluctuations detected in the profilometry data on the film surface are very similar to those seen on the substrate surface, indicating that the film growth itself yields smooth films. The SEM image for the same sample is displayed in the inset, showing the homogeneous nature of the films. The grains are well dispersed with an average size of 84 ± 12 nm.

Finally, we like to mention that we carried out very preliminary experiments for other metal precursors in combination with DEZ and observed that similar processes with CuCl₂ and Ni(thd)₂ yielded multimetal (Cu–Zn and Ni–Zn) films as well. Hence, it tentatively seems that the presence of DEZ plays an important role in these processes.

4. DISCUSSION ON THE MECHANISM

We discuss the film growth mechanism based on the DFT calculation results. The proposed plausible ALD reaction steps are shown in Scheme 1; upon adsorption, FeCl₃ has strong exothermic adsorption energy at -4.85 eV, resulting in bond breaking of Fe–Cl. The direct Cl₂ loss has a high energy cost at a value of 4.69 eV. This direct Cl₂ loss is not considered an elimination pathway. Zn(Et)₂ is added to the surface, resulting in exothermic reaction energy at -5.87 eV. The structures of FeCl₃ adsorption and Zn(Et)₂ adsorption on the Fe₄Zn₉(100) surface are shown in Figure 6.

We then simulated three plausible pathways, as shown in Scheme 1, and plotted the corresponding reaction pathways in Figure 7. We first focused on introducing one FeCl₃ and one

Scheme 1. Illustration of the Proposed Reaction Steps between FeCl_3 and $\text{Zn}(\text{Et})_2$ ^a

^a(I) Initial surface reaction of FeCl_3 results in $-\text{FeCl}_2$ and $-\text{Cl}$ on the surface. (II) Initial surface reaction of $\text{Zn}(\text{Et})_2$ results in physisorption of $\text{Zn}(\text{Et})_2$. (III) Ligand elimination pathway via EtCl loss. (IV) Ligand elimination pathway via butane loss and ZnCl_2 loss. (V) Ligand elimination pathway via butane loss and Cl_2 loss.

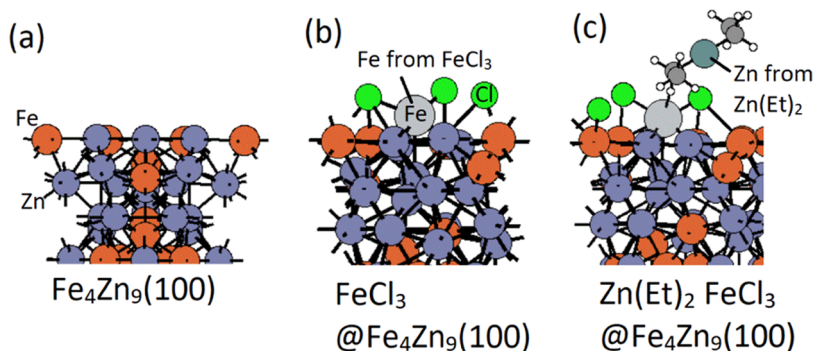


Figure 6. Structures of (a) slab model of $\text{Fe}_4\text{Zn}_9(100)$, (b) FeCl_3 adsorption on $\text{Fe}_4\text{Zn}_9(100)$, and (c) $\text{Zn}(\text{Et})_2$ and FeCl_3 coadsorption on $\text{Fe}_4\text{Zn}_9(100)$. Substrate Zn and Fe atoms are represented by dark gray and orange colors, Zn and Fe from precursors by dark green and light gray colors, and C, H, and Cl by black, white, and green colors.

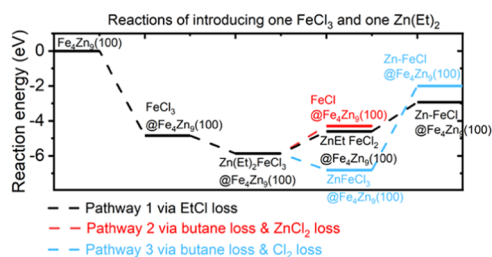


Figure 7. Plotted reaction energy pathways for eliminating the Cl group and the Et ligand via pathways 1, 2, and 3.

$\text{Zn}(\text{Et})_2$ precursor. Pathway 1 via EtCl loss is the most exothermic reaction pathway, with computed overall reaction energy at -4.61 eV for the first EtCl loss and -2.94 eV for the second EtCl loss. Pathways 2 and 3 contain butane loss. For pathway 2, in addition to butane, a Cl group is eliminated via ZnCl_2 loss, resulting in higher overall reaction energy at -4.29 eV. This pathway is not considered due to no Zn deposition on the surface. Pathway 3 has byproducts of butane and Cl_2 . After

Cl_2 loss, the computed overall reaction energy is -2.00 eV. Pathway 3 has a high energy cost of 4.81 eV to lose Cl_2 . The remaining Cl groups for pathways 1 and 3 can be removed through interaction with another $\text{Zn}(\text{Et})_2$ reducing agent in the DEZ pulse.

After the first $\text{Zn}(\text{Et})_2$ adsorption and reaction, the surface has one Cl group left for pathway 1 and three Cl groups for pathway 3. We then bring in the second $\text{Zn}(\text{Et})_2$ reducing agent. As shown in Figure 8, for pathway 1, the second $\text{Zn}(\text{Et})_2$ has an exothermic interaction energy of -4.11 eV and the loss of the Cl group is exothermic at -4.16 eV. The structures after interaction with two $\text{Zn}(\text{Et})_2$ are shown for pathway 1 in Figure 9.

For pathway 3, the second $\text{Zn}(\text{Et})_2$ has exothermic adsorption energy at -7.76 eV and the loss of two Cl groups via EtCl loss results in exothermic reaction energy at -5.73 eV. The structures after the first $\text{Zn}(\text{Et})_2$ reaction and the second $\text{Zn}(\text{Et})_2$ reaction are shown in Figure 10 for pathway 3. These energies are more exothermic than overall reaction energies from pathway 1.

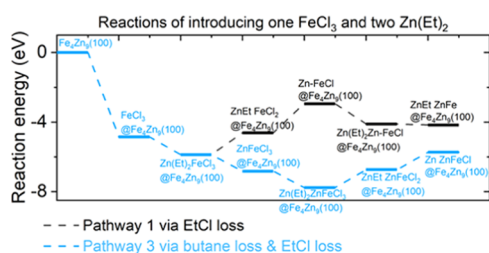


Figure 8. Plotted reaction energy pathways for eliminating the Cl group and the Et ligand via pathways 1 and 3 after introducing two $\text{Zn}(\text{Et})_2$ reducing agents.

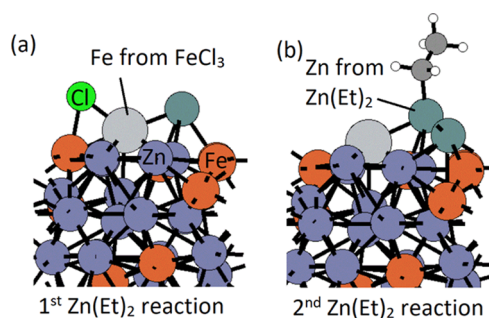


Figure 9. Structures of after ligand elimination of introducing the (a) first $\text{Zn}(\text{Et})_2$ reducing agent and (b) second $\text{Zn}(\text{Et})_2$ reducing agent via pathway 1. Substrate Zn and Fe atoms are represented by dark gray and orange colors, Zn and Fe from precursors by dark green and light gray colors, and C, H, and Cl by black, white, and green colors.

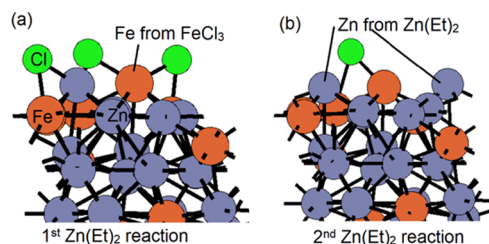


Figure 10. Structures of after ligand elimination of introducing the (a) first $\text{Zn}(\text{Et})_2$ reducing agent and (b) second $\text{Zn}(\text{Et})_2$ reducing agent via pathway 3. Zn and Fe atoms are represented by dark gray and orange colors. Cl is represented by green color.

We conclude that the elimination mechanism of the Cl group and the Et ligand is via butane loss and EtCl loss, by introducing one FeCl_3 and two $\text{Zn}(\text{Et})_2$. The remaining Cl group or Et ligand will be eliminated through an additional $\text{Zn}(\text{Et})_2$ in this pulse. The composition of deposited intermetallic Fe–Zn can then be manipulated by controlling the precursor concentration.

5. CONCLUSIONS

This paper reports a new ALD scheme for the growth of metal alloy/intermetallic thin films. No additional/actual reductant such as hydrogen or hydrides is employed; instead, the two metal precursors react directly to yield both the metal species in a metallic form. Our detailed experimental data are for the intermetallic $\gamma\text{-Fe}_4\text{Zn}_9$ phase obtained from the $\text{FeCl}_3 + \text{Zn}(\text{CH}_2\text{CH}_3)_2$ process. However, our preliminary tests suggested that similar processes could be possibly developed for other metal precursors as well, in combination with DEZ.

From the detailed process parameter investigation for the $\text{FeCl}_3 + \text{DEZ}$ process, we could conclude that the process fulfills the basic criteria of an ALD process, that is, the surface-limited and linear (against the number of precursor supply cycles) film growth. Computational DFT calculations indicated that the favorable pathway of eliminating the Cl group and the Et ligand is via butane and subsequent EtCl formation and desorption.

All of the films were crystalline of the $\gamma\text{-Fe}_4\text{Zn}_9$ phase, with traces of the $\alpha\text{-Fe}$ phase in some samples. Depending on the process parameters, some variation was seen in the degree of crystallinity and also in the Fe/Zn ratio. While not challenged in this work, these intermetallic films could be beneficial, e.g., as biodegradable implant coatings, or in other frontier applications motivated by the simplicity of the fabrication process based on only two well-known ALD precursors. We foresee that the new ALD scheme presented here will trigger the research on the emerging field of high-quality (multi)metal thin films.

AUTHOR INFORMATION

Corresponding Author

Maarit Karppinen – Department of Chemistry and Materials Science, Aalto University, FI-00076 Espoo, Finland;
 orcid.org/0000-0003-1091-1169;
 Email: maarit.karppinen@aalto.fi

Authors

Ramin Ghiyasi – Department of Chemistry and Materials Science, Aalto University, FI-00076 Espoo, Finland
 Anish Philip – Department of Chemistry and Materials Science, Aalto University, FI-00076 Espoo, Finland;
 orcid.org/0000-0001-9978-210X
 Ji Liu – Tyndall National Institute, UCC, Cork T12 R5CP, Ireland; orcid.org/0000-0001-7190-9869
 Jaakko Julin – Department of Physics, University of Jyväskylä, FI-40014 Jyväskylä, Finland; orcid.org/0000-0003-4376-891X
 Timo Sajavaara – Department of Physics, University of Jyväskylä, FI-40014 Jyväskylä, Finland
 Michael Nolan – Tyndall National Institute, UCC, Cork T12 R5CP, Ireland; orcid.org/0000-0002-5224-8580

Complete contact information is available at:
<https://pubs.acs.org/10.1021/acs.chemmater.2c00907>

Author Contributions

This manuscript was written through contributions of all authors.

Notes

The authors declare no competing financial interest.

ACKNOWLEDGMENTS

This project has received funding from the European Union's Horizon 2020 Research and Innovation Programme under the Marie Skłodowska-Curie grant agreement (Grant No. 765378) and the Academy of Finland (Flagship PREIN). A.P. gratefully acknowledges the PoDoCo funding by the Finnish Foundation for Technology Promotion. J.L. and M.N. acknowledge funding support from the Science Foundation Ireland through the SFI-NSF China Partnership, Grant No. 17/NSFC/5279. The authors also gratefully acknowledge the use of the RawMatters Finland Infrastructure (RAMI) at Aalto University

and support and computational resources from the Irish Centre for High-End Computing (ICHEC) and the SFI funded Tyndall computing resources.

REFERENCES

- (1) Suntola, T. Atomic layer epitaxy. *Mater. Sci. Rep.* **1989**, *4*, 261–312.
- (2) George, S. M. Atomic layer deposition: an overview. *Chem. Rev.* **2010**, *110*, 111–131.
- (3) Leskelä, M.; Ritala, M. Atomic layer deposition (ALD): from precursors to thin film structures. *Thin Solid Films* **2002**, *409*, 138–146.
- (4) Johnson, R. W.; Hultqvist, A.; Bent, S. A brief review of atomic layer deposition: from fundamentals to applications. *Mater. Today* **2014**, *17*, 236–246.
- (5) Van Bui, H.; Grillo, F.; van Ommen, J. R. Atomic and molecular layer deposition: off the beaten track. *Chem. Commun.* **2017**, *53*, 45–71.
- (6) Zhang, Z.; Zhao, Y.; Zhao, Z.; Huang, G.; Mei, Y. Atomic layer deposition-derived nanomaterials: oxides, transition metal dichalcogenides, and metal–organic frameworks. *Chem. Mater.* **2020**, *32*, 9056–9077.
- (7) Richey, N. E.; de Paula, C.; Bent, S. F. Understanding chemical and physical mechanisms in atomic layer deposition. *J. Chem. Phys.* **2020**, *152*, No. 040902.
- (8) Sønsteby, H. H.; Yanguas-Gil, A.; Elam, J. W. Consistency and reproducibility in atomic layer deposition. *J. Vac. Sci. Technol. A* **2020**, *38*, No. 020804.
- (9) Niemelä, J.-P.; Marin, G.; Karppinen, M. Titanium dioxide thin films by atomic layer deposition: a review. *Semicond. Sci. Technol.* **2017**, *32*, No. 093005.
- (10) Tynell, T.; Karppinen, M. Atomic layer deposition of ZnO: a review. *Semicond. Sci. Technol.* **2014**, *29*, No. 043001.
- (11) Tripathi, T. S.; Lahtinen, J.; Karppinen, M. Atomic layer deposition of conducting CuS thin films from elemental sulfur. *Adv. Mater. Interfaces* **2018**, *5*, No. 1701366.
- (12) Meng, X.; Byun, Y.-C.; Kim, H. S.; Lee, J. S.; Lucero, A. T.; Cheng, L.; Kim, J. Atomic layer deposition of silicon nitride thin films: a review of recent progress, challenges, and outlooks. *Materials* **2016**, *9*, No. 1007.
- (13) Seim, H.; Mölsä, H.; Nieminen, M.; Fjellvåg, H.; Niinistö, L. Deposition of LaNiO₃ thin films in an atomic layer epitaxy reactor. *J. Mater. Chem.* **1997**, *7*, 449–454.
- (14) Ahvenniemi, E.; Matvejeff, M.; Karppinen, M. Atomic layer deposition of quaternary oxide (La,Sr)CoO_{3-δ} thin films. *Dalton Trans.* **2015**, *44*, 8001–8006.
- (15) Mackus, A. J. M.; Schneider, J. R.; MacIsaac, C.; Baker, J. G.; Bent, S. F. Synthesis of doped, ternary, and quaternary materials by atomic layer deposition: a review. *Chem. Mater.* **2019**, *31*, 1142–1183.
- (16) Hämäläinen, J.; Ritala, M.; Leskelä, M. Atomic layer deposition of noble metals and their oxides. *Chem. Mater.* **2014**, *26*, 786–801.
- (17) Hagen, D. J.; Pemble, M. E.; Karppinen, M. Atomic layer deposition of metals: precursors and film growth. *Appl. Phys. Rev.* **2019**, *6*, No. 041309.
- (18) Aaltonen, T.; Ritala, M.; Arstila, K.; Keinonen, J.; Leskelä, M. Atomic layer deposition of ruthenium thin films from Ru(thd)₃ and oxygen. *Chem. Vap. Deposition* **2004**, *10*, 215–219.
- (19) Martensson, P.; Carlsson, J.-O. Atomic layer epitaxy of copper growth and selectivity in the Cu(II)-2,2,6,6-tetramethyl-3,5-heptanedionate/H₂ process. *J. Electrochem. Soc.* **1998**, *145*, 2929–2931.
- (20) Profijt, H. B.; Potts, S. E.; van de Sanden, M. C. M.; Kessels, W. M. M. Plasma-assisted atomic layer deposition: basics, opportunities, and challenges. *J. Vac. Sci. Technol. A* **2011**, *29*, No. 050801.
- (21) Tripathi, T. S.; Karppinen, M. Efficient process for direct ALD of metallic Cu thin films based on an organic reductant. *Chem. Mater.* **2017**, *29*, 1230–1235.
- (22) Tripathi, T. S.; Wilken, M.; Hoppe, C.; de los Arcos, T.; Grundmeier, G.; Devi, A.; Karppinen, M. Atomic layer deposition of copper metal films from Cu(acac)₂ and hydroquinone reductant. *Adv. Eng. Mater.* **2021**, *23*, No. 2100446.
- (23) Christensen, S. T.; Elam, J. W. Atomic layer deposition of Ir-Pt alloy films. *Chem. Mater.* **2010**, *22*, 2517–2525.
- (24) Väyrynen, K.; Hatanpää, T.; Mattinen, M.; Mizohata, K.; Meinander, K.; Räisänen, J.; Link, J.; Stern, R.; Ritala, M.; Leskelä, M. Atomic layer deposition of intermetallic Co₃Sn₂ and Ni₃Sn₂ thin films. *Adv. Mater. Interfaces* **2019**, *6*, No. 1801291.
- (25) Väyrynen, K.; Vihervaara, A.; Hatanpää, T.; Mattinen, M.; Heikkilä, M. J.; Mizohata, K.; Räisänen, J.; Ritala, M.; Leskelä, M. Nickel germanide thin films by atomic layer deposition. *Chem. Mater.* **2019**, *31*, 5314–5319.
- (26) Nieminen, H.-E.; Kaipio, M.; Ritala, M. In situ reaction mechanism study on atomic layer deposition of intermetallic Co₃Sn₂ thin films. *Chem. Mater.* **2020**, *32*, 8120–8128.
- (27) Blakeney, K. J.; Winter, C. H. Atomic layer deposition of aluminum metal films using a thermally stable aluminum hydride reducing agent. *Chem. Mater.* **2018**, *30*, 1844–1848.
- (28) Lee, B. H.; Hwang, J. K.; Nam, J. W.; Lee, S. U.; Kim, J. T.; Koo, S.-M.; Baunemann, A.; Fischer, R. A.; Sung, M. M. Low-temperature atomic layer deposition of copper metal thin films: self-limiting surface reaction of copper dimethylamino-2-propoxide with diethylzinc. *Angew. Chem., Int. Ed.* **2009**, *48*, 4536–4539.
- (29) Vidjayacoumar, B.; Emslie, D. J. H.; Clendenning, S. B.; Blackwell, J. M.; Britten, J. F.; Rheingold, A. Investigation of AlMe₃, BEt₃, and ZnEt₂ as co-reagents for low-temperature copper metal ALD/pulsed-CVD. *Chem. Mater.* **2010**, *22*, 4844–4853.
- (30) Zhong, Z.; Wang, X.; Ding, J.; Yuan, N. Nanometer-thick copper films grown by thermal atomic layer deposition. *Thin Solid Films* **2015**, *589*, 673–680.
- (31) Dey, G.; Elliott, S. D. Mechanism for the atomic layer deposition of copper using diethylzinc as the reducing agent: a density functional theory study using gas-phase molecules as a model. *J. Phys. Chem. A* **2012**, *116*, 8893–8901.
- (32) Klug, J. A.; Becker, N. G.; Riha, S. C.; Martinson, A. B. F.; Elam, J. W.; Pellinaan, M. J.; Proslie, T. Low temperature atomic layer deposition of highly photoactive hematite using iron(III) chloride and water. *J. Mater. Chem. A* **2013**, *1*, 11607–11613.
- (33) Tanskanen, A.; Mustonen, O.; Karppinen, M. Simple ALD process for ε-Fe₂O₃ thin films. *APL Mater.* **2017**, *5*, No. 056104.
- (34) Xiang, J.; Ding, Y.; Du, L.; Xu, C.; Li, T.; Wang, X.; Li, J.; Zhao, C. Investigation of N type metal TiAlC by thermal atomic layer deposition using TiCl₄ and TEA as precursors. *ECS J. Solid State Sci. Technol.* **2016**, *5*, P299–P303.
- (35) Xiang, J.; Li, T.; Zhang, Y.; Wang, X.; Gao, J.; Cui, H.; Yin, H.; Li, J.; Wang, W.; Ding, Y.; Xu, C.; Zhao, C. Investigation of TiAlC by atomic layer deposition as N type work function metal for FinFET. *ECS J. Solid State Sci. Technol.* **2015**, *4*, P441–P444.
- (36) Xiang, J.; Zhang, Y.; Li, T.; Wang, X.; Gao, J.; Yin, H.; Li, J.; Wang, W.; Ding, Y.; Xu, C.; Zhao, C. Investigation of thermal atomic layer deposited TiAlX (X = N or C) film as metal gate. *Solid-State Electron.* **2016**, *122*, 64–69.
- (37) Pore, V.; Hatanpää, T.; Ritala, M.; Leskelä, M. Atomic layer deposition of metal tellurides and selenides using alkylsilyl compounds of tellurium and selenium. *J. Am. Chem. Soc.* **2009**, *131*, 3478–3480.
- (38) Mita, K.; Ikeda, T.; Maeda, M. Phase diagram study of Fe-Zn intermetallics. *J. Phase Equilib.* **2001**, *22*, 122–125.
- (39) Inui, H.; Okamoto, N. L.; Yamaguchi, S. Crystal structures and mechanical properties of Fe–Zn intermetallic compounds formed in the coating layer of galvanized steels. *ISIJ Int.* **2018**, *58*, 1550–1561.
- (40) Hashizume, Y.; Inamoto, M.; Okamoto, N. L.; Takebayashi, H.; Inui, H. Micropillar compression deformation of single crystals of the intermetallic compound Γ-Fe₄Zn₉. *Acta Mater.* **2020**, *199*, 514–522.
- (41) Yadav, A. P.; Katayama, H.; Noda, K.; Masuda, H.; Nishikata, A.; Tsuru, T. Effect of Fe–Zn alloy layer on the corrosion resistance of galvanized steel in chloride containing environments. *Corros. Sci.* **2007**, *49*, 3716–3731.

(42) Panagopoulos, C. N.; Georgiou, E. P.; Agathocleous, P. E.; Giannakopoulos, K. I. Mechanical behaviour of Zn–Fe alloy coated mild steel. *Mater. Des.* **2009**, *30*, 4267–4272.

(43) Kafri, A.; Ovardia, S.; Yosafovich-Doitch, G.; Aghion, E. In vivo performances of pure Zn and Zn-Fe alloy as biodegradable implants. *J. Mater. Sci. Mater. Med.* **2018**, *29*, No. 94.

(44) Kabir, H.; Munir, K.; Wen, C.; Li, Y. Recent research and progress of biodegradable zinc alloys and composites for biomedical applications: biomechanical and biocorrosion perspectives. *Bioact. Mater.* **2021**, *6*, 836–879.

(45) Kresse, G.; Joubert, D. From ultrasoft pseudopotentials to the projector augmented-wave method. *Phys. Rev. B* **1999**, *59*, 1758–1775.

(46) Perdew, J. P.; Chevary, J. A.; Vosko, S. H.; Jackson, K. A.; Pederson, M. R.; Singh, D. J.; Fiolhais, C. Atoms, molecules, solids, and surfaces: Applications of the generalized gradient approximation for exchange and correlation. *Phys. Rev. B* **1992**, *46*, 6671–6687.

(47) Perdew, J. P.; Burke, K.; Ernzerhof, M. Generalized gradient approximation made simple. *Phys. Rev. Lett.* **1996**, *77*, 3865–3868.

(48) Monkhorst, H. J.; Pack, J. D. Special points for Brillouin-zone integrations. *Phys. Rev. B* **1976**, *13*, 5188–5192.

(49) Libera, J. A.; Elam, J. W.; Pellin, M. J. Conformal ZnO coatings on high surface area silica gel using atomic layer deposition. *Thin Solid Films* **2008**, *516*, 6158–6166.

(50) Johansson, A.; Ljung, H.; Westman, S. X-ray and neutron diffraction studies on C-Ni, Zn and C-Fe, Zn. *Acta Chem. Scand.* **1968**, *22*, 2743–2753.

(51) Wilburn, D. R.; Bassett, W. A. Hydrostatic compression of iron and related compounds: an overview, $P = 1$. *Am. Mineral.* **1978**, *63*, 591–596.

Recommended by ACS

Iron-Intercalated Zirconium Diselenide Thin Films from the Low-Pressure Chemical Vapor Deposition of $[\text{Fe}(\eta^5\text{-C}_5\text{H}_4\text{Se})_2\text{Zr}(\eta^5\text{-C}_5\text{H}_5)_2]_2$

Clara Sanchez-Perez, Claire J. Carmalt, *et al.*

JUNE 24, 2020
ACS OMEGA

READ [↗](#)

Atomic Layer Deposition of FeSe_2 , CoSe_2 , and NiSe_2

Zheng Guo, Xinwei Wang, *et al.*

APRIL 01, 2021
CHEMISTRY OF MATERIALS

READ [↗](#)

Molecular Mechanism of Thermal Dry Etching of Iron in a Two-Step Atomic Layer Etching Process: Chlorination Followed by Exposure to Acetylacetone

Mahsa Konh, Andrew Teplyakov, *et al.*

MARCH 26, 2021
THE JOURNAL OF PHYSICAL CHEMISTRY C

READ [↗](#)

High-Throughput Characterization of $(\text{Fe}_x\text{Co}_{1-x})_3\text{O}_4$ Thin-Film Composition Spreads

Tobias H. Piotrowiak, Alfred Ludwig, *et al.*

NOVEMBER 05, 2020
ACS COMBINATORIAL SCIENCE

READ [↗](#)

Get More Suggestions >